IOP Publishing Phys. Med. Biol. 63 (2018) 025007 (13pp) https://doi.org/10.1088/1361-6560/aa9cfe

Physics in Medicine & Biology

IPEM Institute of Physics and Engineering in Medicine

PAPER

Diffusion tensor optical coherence tomography

Daniel L Marks[1], Richard L Blackmon[2] and Amy L Oldenburg[2,3]

[1] Department of Electrical and Computer Engineering, Duke University, 101 Science Drive, Durham NC 27708, United States of America
[2] Department of Physics and Astronomy, University of North Carolina at Chapel Hill, Chapel Hill, NC 27599, United States of America
[3] Biomedical Research Imaging Center, University of North Carolina at Chapel Hill, Chapel HIll, NC 27599, United States of America

E-mail: aold@physics.unc.edu

RECEIVED
16 June 2017

REVISED
20 September 2017

ACCEPTED FOR PUBLICATION
24 November 2017

PUBLISHED
9 January 2018

Keywords: diffusion tensor imaging, optical coherence tomography, anisotropic diffusion, dynamic light scattering

Abstract

In situ measurements of diffusive particle transport provide insight into tissue architecture, drug delivery, and cellular function. Analogous to diffusion-tensor magnetic resonance imaging (DT-MRI), where the anisotropic diffusion of water molecules is mapped on the millimeter scale to elucidate the fibrous structure of tissue, here we propose diffusion-tensor optical coherence tomography (DT-OCT) for measuring directional diffusivity and flow of optically scattering particles within tissue. Because DT-OCT is sensitive to the sub-resolution motion of Brownian particles as they are constrained by tissue macromolecules, it has the potential to quantify nanoporous anisotropic tissue structure at micrometer resolution as relevant to extracellular matrices, neurons, and capillaries. Here we derive the principles of DT-OCT, relating the detected optical signal from a minimum of six probe beams with the six unique diffusion tensor and three flow vector components. The optimal geometry of the probe beams is determined given a finite numerical aperture, and a high-speed hardware implementation is proposed. Finally, Monte Carlo simulations are employed to assess the ability of the proposed DT-OCT system to quantify anisotropic diffusion of nanoparticles in a collagen matrix, an extracellular constituent that is known to become highly aligned during tumor development.

1. Introduction

Living tissue contains aqueous intra- and extra-cellular spaces where particles undergo Brownian motion (self-diffusion). As particles collide with tissue macromolecules or surfaces, their diffusion is hindered. In tissues with aligned fibers or elongated pores, particle diffusion becomes anisotropic and is best described by a diffusion tensor. The ability to image the diffusion tensor has revealed many new insights into *in vivo* tissue ultrastructure. The best-known example is DT-MRI (Basser *et al* 1994, Le Bihan *et al* 2001, Melhem *et al* 2002, Mori and Zhang 2006, Mukherjee *et al* 2008, Mori and Tournier 2014), in which the diffusion tensor of water molecules is mapped to infer the direction and connectivity of neuronal tracts in the brain. However, the heterogeneity of tissue causes the typically millimeter-resolution DT-MRI to be volume-averaged over multiple tissue components with varying diffusion tensors, while better resolution can only be accomplished with excessively long scan times (Le Bihan *et al* 2001). To resolve structural heterogeneity on the cellular scale, dynamic light scattering optical coherence tomography (DLS-OCT) is of growing interest. DLS-OCT measures the coherence-gated diffusion rate of optically scattering particles along the direction of a single probe beam with a resolution on the order of 10 μm (Boas *et al* 1998). While DLS-OCT has been predominantly used in conjunction with flow measurements in blood vessels (Lee *et al* 2012), it has also been applied for spatially-resolved microrheology (Popescu *et al* 2002, Chhetri *et al* 2011). Recently, we have developed a type of DLS-OCT to resolve tissue porosity (i.e. pore size) by employing plasmonic gold nanorods sensitive to nanoscale pores by merit of their constrained diffusion, and applied the method to study mucus hydration and extracellular matrix (ECM) remodeling *in vitro* (Chhetri *et al* 2014, Blackmon *et al* 2016, 2017). However, tissues are rarely isotropic in structure, and a single diffusion constant D is insufficient to describe particle transport. Here we propose diffusion tensor optical coherence tomography (DT-OCT) to obtain the coherence-gated diffusion tensor $\bar{\bar{\mathbf{D}}}$ to specify diffusion in all directions. Because $\bar{\bar{\mathbf{D}}}$ is a symmetric, second-order tensor, in three dimensions it is uniquely determined by six components. To completely

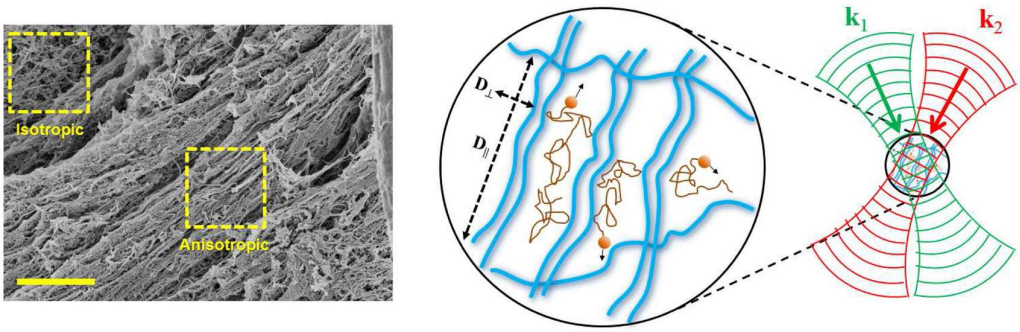

Figure 1. DT-OCT concept diagram. Left: electron microscopy of artificial ECM after remodeling by stromal fibroblasts *in vitro* shows heterogeneity of fiber alignment (boxed regions and scalebar 6 μm). Middle: diffusion of nanoparticles in an anisotropic medium is larger in the direction parallel to the long axis of the pores. Right: OCT beams that probe a volume at different angles are used to measure the component of diffusion along each wave vector **k**, noting that the wavefront of each beam is flat near the focus.

characterize the tensor, a minimum of six measurements of the decorrelation time from different directions using OCT are required. At the same time, the 3 drift velocity components may be independently determined.

The concept of DT-OCT is described in figure 1. Self-diffusing particles intermittently collide with macromolecules such that D is reduced from that in the solvent alone. In anisotropic media with elongated pores, particle diffusion is higher in the direction of pore elongation, $D_\parallel$, and lower in the direction of pore contraction, $D_\perp$. A major application of DT-OCT would be to quantify the 3D anisotropy of pores in ECM as it relates to the progression of breast cancer. The structural and mechanical properties of mammary ECM are modified by cancer-associated stromal cells (fibroblasts), and can drive the invasiveness of breast cancer (Provenzano *et al* 2006, Cox and Erler 2011, Wolf *et al* 2013). Several methods currently exist to study the structure and micro-mechanics of ECM, including immunofluorescence (Paszek *et al* 2005, Levental *et al* 2009), multiphoton microscopy (Ajeti *et al* 2011), particle tracking rheology (Jones *et al* 2014), and atomic force microscopy (Akhtar *et al* 2009). Our DLS-OCT methods (Chhetri *et al* 2014, Blackmon *et al* 2016) enabled for the first time non-invasive measurements of ECM nanoporosity, but could not reveal the anisotropy of pores. In figure 1 is displayed an artificial ECM remodeled by stromal fibroblasts, revealing how the pore anisotropy increases with increasing stromal cells. Importantly, this pore alignment is 'patchy', i.e. heterogeneous on a micrometer size scale, a feature which can only be captured with the proposed DT-OCT technique, as non-invasive measurements of pore shape at cellular resolutions do not exist. Elucidating pore anisotropy may reveal ordered ECM directionality that is known to influence cell migration (Paszek *et al* 2005, Falzon *et al* 2008, Cox and Erler 2011), and reveal strain on ECM fibers from stromal cells that signal mechanoreceptors on cancer cells (Paszek *et al* 2005, Assoian and Klein 2008, Camp *et al* 2011, Barcus *et al* 2013). As such, DT-OCT represents a new tool for spatially resolving ECM pore sizes and shapes.

DT-OCT proceeds in close analogy with its DT-MRI counterpart. DT-MRI operates by applying a pulse sequence, often a spin-echo pulse, to a population of spins within a magnetic field gradient. Because spin precession rate is determined by the local magnetic field strength, the rate changes as spin moves along the magnetic field gradient. The spin-echo pulse sequence subtracts the precessed transverse magnetization phase in the interval after the 180° phase-reflecting pulse with that occurring before the pulse. In the absence of motion of the spin, the precession phase accumulations before and after the 180° pulse exactly cancel, resulting in a strong echo pulse. However, if the spin moves along the magnetic field gradient, the precession rate is different before and after the 180° pulse, causing a nonzero phase accumulation that modulates the echo pulse. The net phase accumulation is proportional to the difference in magnetic fields at the spin's start and end positions. Therefore the motion of the spin due to drift or diffusion is encoded onto the phase of the echo signal. Drift is encoded into a phase proportional to the component of the velocity along the gradient. As the motion of diffusion is random, the sum of random phases from multiple particle motions results in the decay of the spin echo signal with increasing precession time. By using two or more spin-echo pulses with different precession time intervals, the exponential decay rate of the echo signal may be ascertained, with a greater decay rate indicating more spins that diffuse more readily. In practice, the 'b-matrix' (Mattiello *et al* 1994) of a pulse sequence is tailored to select the directions most sensitive to spin motion based on the directions of applied magnetic field gradients. By measuring with many pulse sequences that probe different directions, the diffusion rate in these directions may be calculated from the measured echo decay rates. These diffusion rates are then combined to estimate the diffusion tensor.

DT-OCT is similarly able to quantify the drift and diffusion of particles. Like its DT-MRI counterpart, to determine the motions of a particle using OCT, the backscattered OCT signals captured at two or more time intervals are compared, although unlike MRI, they are correlated in post-processing. At an initial time, the posi-

tion of a particle is encoded onto the phase of the backscattered signal. At a later time, drift and diffusion have moved the particle and a new position is encoded onto the phase. The difference between these two optical phases is analogous to the residual phase encoded onto a moving spin after a spin-echo pulse sequence. The gradient of the phase difference between the incident and scattered electromagnetic fields, that is, the difference of the incident and scattered wave vectors, is analogous to the applied magnetic field gradient of MRI for determining in which direction particle motion is detected. Drift, or the motion of the particle at a uniform speed in a particular direction, produces a periodic modulation of the phase which is the conventional Doppler shift as measured by OCT. Diffusion, which is caused by solvent molecules randomly colliding with the particle, displaces the particle in a random direction with a mean-squared displacement proportional to the time between observations. Unlike drift which produces a deterministic phase variation of the backscattered signal, the signal variation due to diffusion becomes exponentially decorrelated as time progresses, just as for MRI. Because OCT can acquire axial scans at rates exceeding tens of kHz, an autocorrelation of the backscattered signal may be estimated on time scales over many orders of magnitude. The decorrelation time may be characterized by fitting an exponential decay time constant τ to the autocorrelation of the backscattered OCT signal. With knowledge of the center wavelength λ of the illumination, refractive index n, and the corresponding scattering vector $q = 4\pi n/\lambda$, the diffusion constant is estimated as $D = 1/\tau q^2$. This diffusion constant, for isotropic media, parameterizes the probability distribution of the particle's position as time progresses, as described by the Fokker–Planck equation.

In this paper we develop the theory of anisotropic diffusion and drift in the frequency-domain in section 2. The autocorrelation of the backscattered optical signal from diffusing and drifting particles in a coherence volume is then derived in section 3. In section 4, it is explained how to find the linear equations that relate the components of the drift velocity and diffusion tensor to the decay times. In section 5, the six optical illumination directions for best estimating the diffusion tensor are determined through numerical optimization given a finite numerical aperture, and in section 6, an example hardware implementation for rapidly assessing tissue along these six directions is proposed. A simple example of DT-OCT of axisymmetric diffusion is given in sections 7, and in 8, Monte Carlo simulations are performed to simulate DT-OCT measurements of nanoparticles diffusing in ECM with anisotropic, axisymmetric pores.

2. Frequency-domain drift and diffusion

To determine the backscattered optical signal that is received from a population of particles undergoing drift and diffusion, it is convenient to first solve for the frequency-domain or Fourier transform of the particle density. It is assumed that the diffusion tensor and drift velocity in the medium are slowly varying relative to the spatial scale of the particle concentration gradient. This is a transient analysis that assumes an initial condition, however, the transient analysis also models temporal fluctuations of the particle density due to thermal excitations and therefore is subsequently used to calculate the correlations in particle density with time. Furthermore, collisions between particles are neglected and so the particles diffuse independently. We start with Fick's law applied to a time-dependent particle density $\rho(\mathbf{r})$, given a diffusion tensor field $\bar{\bar{\mathbf{D}}}$, drift velocity field $\mathbf{v}$, and a time-dependent particle flux $\mathbf{J}$, all functions of position $\mathbf{r}$ in the medium:

$$\mathbf{J} = -\bar{\bar{\mathbf{D}}}\nabla\rho + \mathbf{v}\rho. \tag{1}$$

In this derivation, the ∇ gradient operator is the column vector $\left[\frac{\partial}{\partial x}\frac{\partial}{\partial y}\frac{\partial}{\partial z}\right]^T$, ∇^T is the divergence operator row vector $\left[\frac{\partial}{\partial x}\frac{\partial}{\partial y}\frac{\partial}{\partial z}\right]$ applied to each column of a matrix or vector, and $\nabla\nabla^T$ is the Hessian matrix operator which is each element of the Hessian matrix applied to a scalar. The diffusion equation is derived by applying particle conservation $\nabla^T\mathbf{J} + \frac{\partial\rho}{\partial t} = 0$:

$$-\mathrm{tr}\ \bar{\bar{\mathbf{D}}}\nabla\nabla^T\rho - \nabla^T\bar{\bar{\mathbf{D}}}\nabla\rho + \mathbf{v}^T\nabla\rho + \rho\nabla^T\mathbf{v} + \frac{\partial\rho}{\partial t} = 0. \tag{2}$$

If the diffusion tensor and velocity field are slowly spatially varying compared to the particle concentration gradient, then:

$$\frac{\left|\nabla^T\bar{\bar{\mathbf{D}}}\right|}{\left|\bar{\bar{\mathbf{D}}}\right|} \ll \frac{|\nabla\rho|}{|\rho|} \text{ and } \frac{\left|\nabla^T\mathbf{v}\right|}{|\mathbf{v}|} \ll \frac{|\nabla\rho|}{|\rho|}, \tag{3}$$

and the $\nabla^T\bar{\bar{\mathbf{D}}}\nabla\rho$ and $\rho\nabla^T\mathbf{v}$ terms may be omitted:

$$-\mathrm{tr}\ \bar{\bar{\mathbf{D}}}\nabla\nabla^T\rho + \mathbf{v}^T\nabla\rho + \frac{\partial\rho}{\partial t} = 0. \tag{4}$$

To solve for the particle density, we use its Fourier transform:

$$\tilde{\rho}(\mathbf{q},t) = \int_V \mathrm{d}^3 r\ \rho(\mathbf{r},t) \exp\left(\mathrm{i}\mathbf{r}^T\mathbf{q}\right), \tag{5}$$

with V being the domain of integration of the volume containing the particles. This is inserted into equation (4), giving:

$$\mathrm{tr}\ \bar{\bar{\mathbf{D}}}\mathbf{q}\mathbf{q}^T\tilde{\rho} + \mathrm{i}\mathbf{v}^T\mathbf{q}\tilde{\rho} + \frac{\partial\tilde{\rho}}{\partial t} = 0, \tag{6}$$

which may be rewritten as:

$$\frac{\partial\tilde{\rho}}{\partial t} = -\mathbf{q}^T(\mathrm{i}\mathbf{v} + \bar{\bar{\mathbf{D}}}\mathbf{q})\tilde{\rho}, \tag{7}$$

which is solved as an initial value problem with known particle concentration at $t = 0$. The solution for $t \geqslant 0$ is:

$$\tilde{\rho}(\mathbf{q},t) = \tilde{\rho}(\mathbf{q},0) \exp\left[-\mathbf{q}^T(\mathrm{i}\mathbf{v} + \bar{\bar{\mathbf{D}}}\mathbf{q})t\right] u(t), \tag{8}$$

with $u(t)$ being the unit step function as the impulse response to a point of infinite density (a Dirac delta function) should be causal.

For calculating correlations of optical signals in the subsequent section, it is helpful to specify the correlations between particle positions for the initial state $\tilde{\rho}(\mathbf{q},0)$ to estimate the temporal autocorrelation of the particle ensemble. If there are N identical particles at starting points $\mathbf{r}_i$ at time $t = 0$, then:

$$\rho(\mathbf{r},0) = \sum_{i=1}^{N} \delta^{(3)}(\mathbf{r} - \mathbf{r}_i), \tag{9}$$

and the spatial Fourier transform of the initial state is:

$$\tilde{\rho}(\mathbf{q},0) = \sum_{i=1}^{N} \exp\left(\mathrm{i}\mathbf{q}^T\mathbf{r}_i\right). \tag{10}$$

The expected value of the magnitude $\left\langle|\tilde{\rho}(\mathbf{q},0)|^2\right\rangle$ is given by:

$$\begin{aligned}\left\langle|\tilde{\rho}(\mathbf{q},0)|^2\right\rangle &= \left\langle \sum_{i=1}^{N} \exp\left(\mathrm{i}\mathbf{q}^T\mathbf{r}_i\right) \sum_{j=1}^{N} \exp\left(-\mathrm{i}\mathbf{q}^T\mathbf{r}_j\right) \right\rangle \\ &= \sum_{i=1}^{N}\sum_{j=1}^{N} \left\langle \exp\left[\mathrm{i}\mathbf{q}^T\left(\mathbf{r}_i - \mathbf{r}_j\right)\right]\right\rangle \\ &= N + \sum_{i=1}^{N}\sum_{j=1,j\neq i}^{N} \left\langle \exp\left[\mathrm{i}\mathbf{q}^T\left(\mathbf{r}_i - \mathbf{r}_j\right)\right]\right\rangle. \end{aligned} \tag{11}$$

If the particles are assumed to be positioned independently and $|\mathbf{q}| \neq 0$, then $\left\langle \exp\left[\mathrm{i}\mathbf{q}^T\left(\mathbf{r}_i - \mathbf{r}_j\right)\right]\right\rangle = 0$ for $i \neq j$ and therefore $\left\langle|\tilde{\rho}(\mathbf{q},0)|^2\right\rangle = N$.

3. Autocorrelation of the backscattered optical signal

The optical signal backscattered from particles within a coherence-gated volume received by OCT is typically detected interferometrically either using time- or frequency-domain OCT (Leitgeb *et al* 2003). The detected signal is the interference between the light backscattered from the particles and a reference wave, giving rise to the speckled image. As particles move a significant fraction of the wavelength, the speckle fluctuates, giving rise to the dynamic signals that we use to infer drift and diffusion. Optical scattering occurs at discontinuities of the electric susceptibility due to the presence of the particles in an otherwise uniform background medium. Typically the incident field on the particles is a Gaussian beam and the collected scattered signal is the projection onto the same incident field mode (Fercher *et al* 2003, Ralston *et al* 2006). The radius of curvature of a focused beam is infinity at the focus, and so near the focus the incident field mode is approximated by a plane wave with wave vector $\mathbf{k}$ and magnitude $\tilde{E}_0$. For simplicity, each particle is assumed to have an isotropic particle polarizability α so that the medium electric susceptibility is given by $\chi_e = \rho\alpha$ and a scalar field model (no polarization) is used. Given this, the complex-valued monostatic backscattered power measured from the object is given by:

$$s(\mathbf{k},t) = \frac{\epsilon_0\alpha}{2}\int_V \mathrm{d}^3 r\ \rho(\mathbf{r},t)\tilde{E}_0 \exp\left[\mathrm{i}\mathbf{r}^T\mathbf{k}\right] \tilde{E}_0 \exp\left[\mathrm{i}\mathbf{r}^T\mathbf{k}\right]. \tag{12}$$

In practice, the complex-valued signal is inferred from real-valued power measurements by separating a temporal signal and its time-reflected conjugate signal using the Fourier or Hilbert transform. The correlations of the received power at two different time points for a given incident wave vector $\mathbf{k}$ can now be calculated. Consider the autocorrelation of the complex-valued power signal received from the wave vector $\mathbf{k}$ as a function of delay τ:

$$\Gamma(\mathbf{k},\tau) = \int_{-\infty}^{\infty} \mathrm{d}t\ s(\mathbf{k},t)s(\mathbf{k},t+\tau)^*. \tag{13}$$

Inserting the definitions of the signal $s(\mathbf{k},t)$:

$$\begin{aligned}\Gamma(\mathbf{k},\tau) = \frac{\epsilon_0^2\alpha^2\left|\tilde{E}_0\right|^4}{4}\int_{-\infty}^{\infty}\mathrm{d}t \\ \int_V \mathrm{d}^3r\ \rho(\mathbf{r},t)\exp\left[\mathrm{i}2\mathbf{r}^T\mathbf{k}\right] \\ \int_V \mathrm{d}^3r'\ \rho(\mathbf{r}',t+\tau)^*\exp\left[-\mathrm{i}2\mathbf{r}'^T\mathbf{k}\right].\end{aligned} \tag{14}$$

Next, the Fourier transform of $\rho(\mathbf{r},t)$ is inserted from equation (5) as $\rho(\mathbf{r},t) = (2\pi)^{-3}\int \mathrm{d}^3q\ \tilde{\rho}(\mathbf{q},t)\exp\left(-\mathrm{i}\mathbf{r}^T\mathbf{q}\right)$:

$$\begin{aligned}\Gamma(\mathbf{k},\tau) = \frac{\epsilon_0^2\alpha^2\left|\tilde{E}_0\right|^4}{4}(2\pi)^{-6}\int_{-\infty}^{\infty}\mathrm{d}t \\ \int_V \mathrm{d}^3r\ \int \mathrm{d}^3q\ \tilde{\rho}(\mathbf{q},t)\exp\left[-\mathrm{i}\mathbf{r}^T\mathbf{q}\right]\exp\left[\mathrm{i}2\mathbf{r}^T\mathbf{k}\right] \\ \int_V \mathrm{d}^3r'\ \int \mathrm{d}^3q'\ \tilde{\rho}(\mathbf{q}',t+\tau)^*\exp\left[\mathrm{i}\mathbf{r}'^T\mathbf{q}'\right]\exp\left[-\mathrm{i}2\mathbf{r}'^T\mathbf{k}\right].\end{aligned} \tag{15}$$

Interchanging the order of integration between r, q and r', q':

$$\begin{aligned}\Gamma(\mathbf{k},\tau) = \frac{\epsilon_0^2\alpha^2\left|\tilde{E}_0\right|^4}{4}(2\pi)^{-6}\int_{-\infty}^{\infty}\mathrm{d}t \\ \int \mathrm{d}^3q\ \tilde{\rho}(\mathbf{q},t)\int_V \mathrm{d}^3r\ \exp\left[-\mathrm{i}\mathbf{r}^T\mathbf{q}\right]\exp\left[\mathrm{i}2\mathbf{r}^T\mathbf{k}\right] \\ \int \mathrm{d}^3q'\ \tilde{\rho}(\mathbf{q}',t+\tau)^*\int_V \mathrm{d}^3r'\ \exp\left[\mathrm{i}\mathbf{r}'^T\mathbf{q}'\right]\exp\left[-\mathrm{i}2\mathbf{r}'^T\mathbf{k}\right].\end{aligned} \tag{16}$$

The integrals over $\mathbf{r}$ and $\mathbf{r}'$ evaluate to delta functions:

$$\begin{aligned}\Gamma(\mathbf{k},\tau) = \frac{\epsilon_0^2\alpha^2\left|\tilde{E}_0\right|^4}{4}\int_{-\infty}^{\infty}\mathrm{d}t \\ \int \mathrm{d}^3q\ \tilde{\rho}(\mathbf{q},t)\delta^{(3)}\left(\mathbf{q}-2\mathbf{k}\right) \\ \int \mathrm{d}^3q'\ \tilde{\rho}(\mathbf{q}',t+\tau)^*\delta^{(3)}\left(\mathbf{q}'-2\mathbf{k}\right).\end{aligned} \tag{17}$$

The integrals over the delta functions evaluate to:

$$\Gamma(\mathbf{k},\tau) = \frac{\epsilon_0^2\alpha^2\left|\tilde{E}_0\right|^4}{4}\int_{-\infty}^{\infty}\mathrm{d}t\ \tilde{\rho}(2\mathbf{k},t)\tilde{\rho}(2\mathbf{k},t+\tau)^*. \tag{18}$$

Now we insert the solution of equation (8), which is the spatial Fourier transform of the time-varying particle density:

$$\begin{aligned}\Gamma(\mathbf{k},\tau) = \frac{\epsilon_0^2\alpha^2\left|\tilde{E}_0\right|^4}{4}\int_{-\infty}^{\infty}\mathrm{d}t\ \tilde{\rho}(2\mathbf{k},0)\exp\left[-2\mathbf{k}^T(\mathrm{i}\mathbf{v}+2\bar{\bar{\mathbf{D}}}\mathbf{k})t\right]u(t) \\ \tilde{\rho}(2\mathbf{k},0)^*\exp\left[-2\mathbf{k}^T(-\mathrm{i}\mathbf{v}+2\bar{\bar{\mathbf{D}}}\mathbf{k})(t+\tau)\right]u(t+\tau).\end{aligned} \tag{19}$$

As it is assumed that no data is sampled for $t < 0$, the unit step functions enforce that the autocorrelation is taken only over a signal at times $t \geqslant 0$. The unit step functions restrict the integration bounds on time, so that for $\tau > 0$, the bounds are from 0 to ∞:

$$\begin{aligned}\Gamma(\mathbf{k},\tau) &= \frac{\epsilon_0^2\alpha^2\left|\tilde{E}_0\right|^4}{4}\int_0^{\infty}\mathrm{d}t\ \left|\tilde{\rho}(2\mathbf{k},0)\right|^2 e^{-2\mathbf{k}^T(\mathrm{i}\mathbf{v}+2\bar{\bar{\mathbf{D}}}\mathbf{k})t}e^{-2\mathbf{k}^T(-\mathrm{i}\mathbf{v}+2\bar{\bar{\mathbf{D}}}\mathbf{k})(t+\tau)} \\ &= \epsilon_0^2\alpha^2\left|\tilde{E}_0\right|^4\frac{\left|\tilde{\rho}(2\mathbf{k},0)\right|^2}{32\mathbf{k}^T\bar{\bar{\mathbf{D}}}\mathbf{k}}\exp\left[-2\mathbf{k}^T(-\mathrm{i}\mathbf{v}+2\bar{\bar{\mathbf{D}}}\mathbf{k})\tau\right].\end{aligned} \tag{20}$$

Likewise for $\tau < 0$, the bounds are from $-\tau$ to ∞, which results in an autocorrelation function that is the complex conjugate of equation (20). $\left|\tilde{\rho}(2\mathbf{k},0)\right|^2$ is dependent on the initial positions of the particles, but this factor only scales the autocorrelation, as expressed in equation (11), and does not change its rate of decay. Inserting the expected value $\left\langle\left|\tilde{\rho}(2\mathbf{k},0)\right|^2\right\rangle = N$ under the assumption that initial particle positions are uncorrelated into equation (20), it is found that:

$$\Gamma(\mathbf{k},\tau) = \epsilon_0^2\alpha^2\left|\tilde{E}_0\right|^4\frac{N}{32\mathbf{k}^T\bar{\bar{\mathbf{D}}}\mathbf{k}}\exp\left[-2\mathbf{k}^T(-\mathrm{i}\mathbf{v}+2\bar{\bar{\mathbf{D}}}\mathbf{k})\tau\right] \tag{21}$$

for $\tau \geqslant 0$ where N is the number of particles being observed, with $\tau < 0$ being the Hermitian conjugate of the above.

4. Calculating the diffusion tensor and drift velocity from the autocorrelation

To determine the diffusion tensor $\bar{\bar{\mathbf{D}}}$ and the drift vector $\mathbf{v}$, a focus volume is probed from several directions $\mathbf{k}_i$ as shown in figure 1. In practice, the incident angle to the focus is determined by the position of the beam in the entrance pupil of objective. At each position, the interference signal is measured and its sample autocorrelation $\Gamma_i(\mathbf{k}_i, \tau)$ is calculated from the signal samples $s(\mathbf{k}, t)$. Examining the logarithm of $\Gamma_i(\mathbf{k}, \tau)$ measured for each direction $\mathbf{k}_i$:

$$\log \Gamma_i(\mathbf{k}_i, \tau) = -2\mathbf{k}_i^T(-\mathrm{i}\mathbf{v} + 2\bar{\bar{\mathbf{D}}}\mathbf{k}_i)\tau + \log\left[\frac{\epsilon_0^2\alpha^2\left|\tilde{E}_0\right|^4|\tilde{\rho}(2\mathbf{k},0)|^2}{32\mathbf{k}^T\bar{\bar{\mathbf{D}}}\mathbf{k}}\right]. \tag{22}$$

The value of $2\mathbf{k}^T(\mathrm{i}\mathbf{v} + 2\bar{\bar{\mathbf{D}}}\mathbf{k})$ may be estimated by finding the logarithmic derivative, which is called β_i:

$$\frac{1}{\Gamma_i}\frac{\mathrm{d}\Gamma_i}{\mathrm{d}\tau} = \beta_i = -2\mathbf{k}_i^T(-\mathrm{i}\mathbf{v} + 2\bar{\bar{\mathbf{D}}}\mathbf{k}_i). \tag{23}$$

If several β_i are calculated for incident directions $\mathbf{k}_i$, the components of the tensor $\bar{\bar{\mathbf{D}}}$ and the vector $\mathbf{v}$ may be solved for as linear combinations of the β_i. As $\bar{\bar{\mathbf{D}}}$ is a symmetric, real-valued tensor it has six unique components. The drift velocity vector $\mathbf{v}$ has three real components. While there are nine unknowns, the imaginary component of β_i determines the drift velocity components only, while the real part determines the diffusion tensor components only. Therefore six directions are sufficient to reconstruct both the drift and diffusion field. Furthermore, the drift component is linear in $\mathbf{k}$ while the diffusion component is quadratic in $\mathbf{k}$. Therefore drift and diffusion can also be distinguished spectroscopically by probing at two or more wavelength bands with a significant difference between the bands.

5. Choosing the directions of illumination to optimally sample the diffusion tensor

To measure the complete diffusion tensor, a point in the sample must be probed from at least six different directions, as shown in figure 2. Which directions are best to optimize the estimate of the tensor components if the principal axes of the diffusion tensor are unknown? For DT-MRI, common choices of directions include the vertices of polyhedra such as icosahedra, or if more directions are desired, an icosahedral geodesic sampling (Hasan *et al* 2001). However, unlike DT-MRI which can apply a gradient along any direction, DT-OCT is limited to beams delivered within a finite numerical aperture. Given this constraint, a solution is presented that finds an optimized solution for six wave vector directions.

In the absence of drift, the diffusion tensor is related to the β_i by $\beta_i = -4\mathbf{k}_i^T\bar{\bar{\mathbf{D}}}\mathbf{k}_i = -4\mathrm{tr}\ \bar{\bar{\mathbf{D}}}\mathbf{k}_i\mathbf{k}_i^T$. Therefore the $\mathbf{k}_i\mathbf{k}_i^T$ comprise a basis of outer products of the wave vectors over which the diffusion tensor is probed. The $\mathbf{k}_i\mathbf{k}_i^T$ need to span all subspaces of $\bar{\bar{\mathbf{D}}}$ to reconstruct all six unique elements of $\bar{\bar{\mathbf{D}}}$. The degree of orthogonality of a set of basis vectors may be evaluated using the Gramian matrix (Gentle 2007), which has matrix elements that are inner products of the basis vectors. In this case, because the basis consists of outer products $\mathbf{k}_i\mathbf{k}_i^T$, the Gramian matrix $\mathbf{G}$ has its elements given by the inner product of all of the outer product pairs such that $G_{ij} = \mathrm{tr}\ \mathbf{k}_i\mathbf{k}_i^T\left(\mathbf{k}_j\mathbf{k}_j^T\right)^T = \left(\mathbf{k}_i^T\mathbf{k}_j\right)^2$. Given a set of wave vector directions $\mathbf{k}_i$, the determinant of the Gramian matrix is a measure of the orthogonality of the samples of β_i, and maximizing the determinant of $\mathbf{G}$ under a particular set of constraints chooses a set of directions optimized for sampling the diffusion tensor.

With a single finite aperture, the object may be probed from a limited range of directions, with the largest angle subtended to the optical axis limited by the numerical aperture NA of the lens. The directions that may be probed are limited by $k_0\sqrt{\epsilon_r - (NA)^2} \leqslant \mathbf{k}_i^T\hat{\mathbf{z}} \leqslant k_0\sqrt{\epsilon_r}$ with ϵ_r being the medium relative dielectric permittivity, and $\hat{\mathbf{z}}$ being the central axis of the optical illumination system. (Note that one may wish a larger NA to accommodate the beam diameter needed to support the desired focal spot width; here we define the NA as that available for beam steering only). The goal then is to find a set of six vectors $|\mathbf{k}_i| = k_0\sqrt{\epsilon_r}$ such that the determinant of the Gramian $\mathbf{G}$ is maximized under the constraint that $k_0\sqrt{\epsilon_r - (NA)^2} \leqslant \mathbf{k}_i^T\hat{\mathbf{z}} \leqslant k_0\sqrt{\epsilon_r}$. Because an exchange of $\mathbf{k}_i \rightarrow -\mathbf{k}_i$ does not change $\mathbf{G}$, the solutions for $\mathbf{k}_i$ may be limited to a hemisphere with generality. This can be achieved, for example, by setting $\mathbf{k}_i^T\hat{\mathbf{z}} \geqslant 0$ so that all incident directions are in the $+z$ direction.

This problem can be approximately solved using constrained optimization. The function to be optimized is:

$$L = -\log\det\mathbf{G} + \sum_{i=1}^{6}\lambda_i\mathbf{k}_i^T\hat{\mathbf{z}} + \lambda_i'\left|\mathbf{k}_i\right|^2, \tag{24}$$

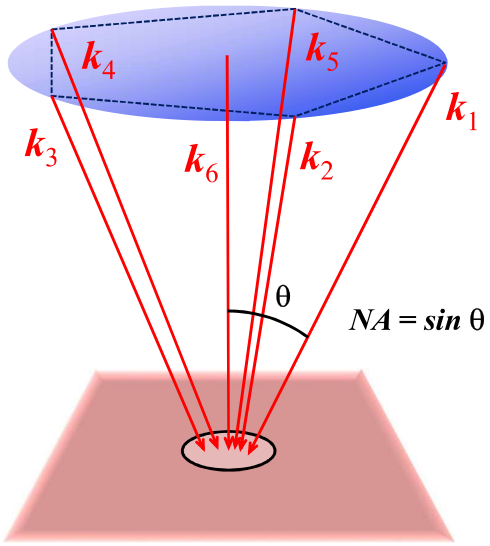

Figure 2. Diagram of a sample being probed from the optimal six different directions for a given NA, with the wave vectors of these directions corresponding to $\mathbf{k}_1$ to $\mathbf{k}_6$.

where λ_i is a Lagrange multiplier that constrains the solutions $\mathbf{k}_i$ to have a positive z component as well as constrains the directions to the given NA, and λ_i' is a Lagrange multiplier to hold the magnitude of $|\mathbf{k}_i|^2 = k_0^2$ so that the same wavelength of illumination is used for all beams. The variation with respect to the $\mathbf{k}_i$ are:

$$\frac{\partial L}{\partial(\mathbf{k}_i^T\hat{\mathbf{n}})} = -\operatorname{tr}\left(\mathbf{G}^{-1}\frac{\partial \mathbf{G}}{\partial(\mathbf{k}_i^T\hat{\mathbf{n}})}\right) + \lambda_i(\hat{\mathbf{n}}^T\hat{\mathbf{z}}) + 2\lambda_i'(\hat{\mathbf{n}}^T\mathbf{k}_i) \tag{25}$$

using Jacobi's formula. To optimize each Cartesian direction, $\hat{\mathbf{x}}$, $\hat{\mathbf{y}}$, or $\hat{\mathbf{z}}$ may be substituted for $\hat{\mathbf{n}}$ to find the variation of L in that particular direction. Using this formula, gradient descent was performed to find a solution for the optimal $\mathbf{k}_i$. After repeated gradient descent optimization starting with random directions, for $NA < 2\sqrt{\epsilon_r/5}$ the solution converged within 10^{-6} accuracy to:

$$\begin{aligned}\mathbf{k}_n &= k_0 NA\left[\cos\left(\tfrac{2\pi}{5}n+\phi_0\right)\hat{\mathbf{x}} + \sin\left(\tfrac{2\pi}{5}n+\phi_0\right)\hat{\mathbf{y}}\right] \\ &\quad + k_0\sqrt{\epsilon_r - (NA)^2}\hat{\mathbf{z}} \text{ for } 1 \leqslant n \leqslant 5 \\ \mathbf{k}_6 &= k_0\sqrt{\epsilon_r}\hat{\mathbf{z}},\end{aligned} \tag{26}$$

where ϕ_0 is an arbitrary angle as the system is rotationally symmetric around $\hat{\mathbf{z}}$. This corresponds to the case shown in figure 2, which has one vector illuminating a point along the z axis, and five equally spaced directions at the edge of the aperture arranged as shown in a pentagon. Valid solutions for $NA \geqslant 2\sqrt{\epsilon_r/5}$ are six vertices on a regular icosahedron arranged such that five of the vertices surround a central vertex, with one solution corresponding to the formula of equation (26) and substituting $NA = 2\sqrt{\epsilon_r/5}$. This is also a solution for DT-MRI where generally there is no constraint on the magnetic field gradient directions as MRI scanners have independently-controlled gradient coils in all three dimensions (Hidalgo-Tobon 2010).

6. Experimental considerations for DT-OCT

In practice, to perform DT-OCT, one must be able to manipulate both the position of the focus and the incident angle of the focused beam. At each position of the focus, an M-scan is acquired at each of a minimum of six different directions of the incident beam (as in figure 2), in order to estimate the diffusion tensor at that position. To probe the components of the drift and diffusion tensor that are perpendicular to the central axis, some of the incident beams must be highly inclined in order to obtain a larger projection of the particle motion along the beam direction. This usually requires a high numerical aperture objective.

One method of independently manipulating both the incident position and angle of the incident beam is to use two sets of galvanometer mirrors in a 4-F system as shown in figure 3 (Goodman 1996). The set of galvos that is conjugate to the front focal plane of the objective lens controls the position of the focus, and the other set of galvos that is conjugate to the image plane controls the direction of the incident angle. It is usually more convenient to have larger diameter, smaller angular range galvanometer mirrors in a high f/# 4-F system, and then to subsequently use a telescope to increase the numerical aperture, demagnify the image, and magnify the incident angle on the sample. To ensure that the beam is incident from different directions into the focus region, the beam

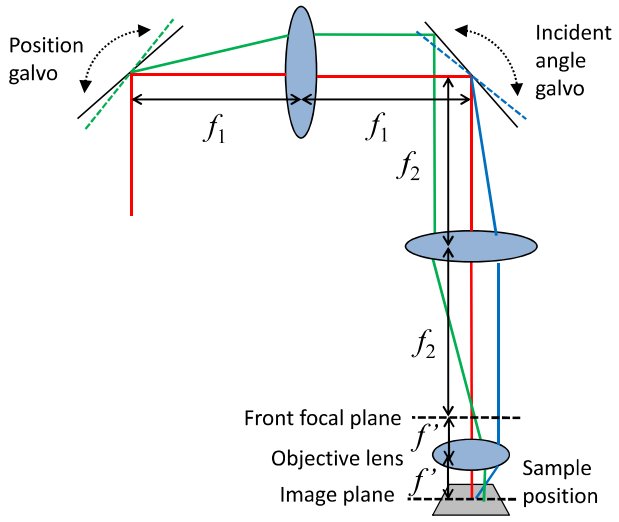

Figure 3. A 4-F system with two galvanometer mirrors, one conjugate to the front focal plane of the objective (position galvo), and the other conjugate to the focus (incident angle galvo), permitting one to independently manipulate the position and incident direction of a focused beam. The red beam travels along the central axis of the system with neither galvo tilted. The green beam is tilted by the position galvo, so that the ray ends up at an off-axis image point. The blue beam is tilted by the incident angle galvo, so it is incident at the image point at an off-axis angle.

should not fill the entrance pupil of the objective. Rather, there should be distinct beam positions in the entrance pupil corresponding to each of the incident direction vectors $\mathbf{k}_i$. An objective with a higher numerical aperture is required than would be needed to achieve a desired transverse resolution as the entire entrance aperture of the objective is not used to focus the beam. We note that the setup of figure 3 is intended to be a simple example of a scanning system capable of acquiring data for DT-OCT, but because several incident angles would be sampled serially, it increases the acquisition time of a DT-OCT image as compared to a conventional OCT image.

Because realistic OCT instruments have ellipsoidally-shaped, finite coherence volumes with the lateral extent determined by transverse resolution Δx and axial resolution Δz, if the observation interval T_{obs} is sufficiently long, particles may enter and exit the coherence volume during the observation interval. When significant numbers of particles transit the coherence volume during the observation time, the autocorrelation decreases more quickly with time than caused by diffusion alone. While models exist for quantifying one-dimensional diffusion in this situation (Popov *et al* 2014), here we will assume that number variations are negligible by placing an upper bound on T_{obs} based upon the transit time:

$$T_{\text{obs}} < \frac{1}{4|v_r|^2}\left(\sqrt{D_r + 4|v_r|\Delta r} - \sqrt{D_r}\right)^2 \Rightarrow \frac{\Delta r^2}{D_r}(|v_r| = 0), \tag{27}$$

where the relation must be met in all directions r with components of drift velocity v_r, diffusion rate D_r, and resolution Δr in that direction.

It is also important to consider the choice of sampling rate and observation time relative to the range of diffusion rates present in the system to be studied. First, the sampling rate (A-line rate) for the M-scans needs to be sufficiently fast relative to the decorrelation rate of the speckle signal. Specifically, this means that the sampling rate, f_s, should be faster than the reciprocal of the $1/e$ decay time of the autocorrelation, or approximately:

$$f_s > 4|k_r|^2 D_r + 2|k_r||v_r|, \tag{28}$$

which must be satisfied for all incident beam directions r and for the largest diffusion rates and drift velocities present in the system. This requirement is already routinely met for DLS-OCT measurements, although it may become challenging for systems with small nanoparticles where diffusivity is high, or in systems with high drift velocities such as in blood. Second, the observation time must be sufficiently long to capture many speckle decorrelation events to obtain sufficient averaging. In practice this suggests that approximately:

$$T_{\text{obs}} \gg 1/(4|k_r|^2 D_r) + 1/(2|k_r||v_r|), \tag{29}$$

which must be satisfied for the smallest diffusion rates and drift velocities present in the system. In practice, we found in our previous DLS-OCT study (in the absence of drift) that T_{obs} needed to 10.75× larger than the decay time for an accurate determination of the diffusion rate (Blackmon *et al* 2017).

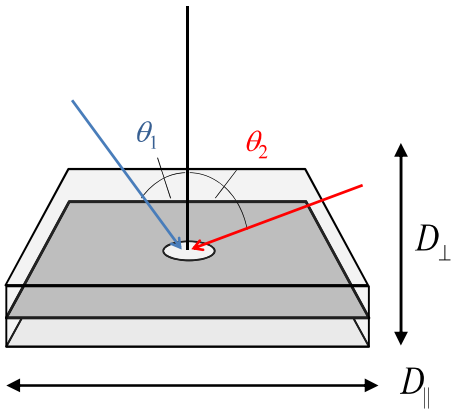

Figure 4. Diagram of a simple example of DT-OCT by probing a point in a medium with two different incident angles θ_1 and θ_2. The diffusion constant in the plane is $D_\parallel$ and perpendicular to the plane is $D_\perp$.

Finally, we note that for an accurate measurement of drift velocity, it must be sufficiently large such relative to diffusion such that the particle's displacement over the observation time has significant components of directed and diffuse travel. Specifically, this means that:

$$|v_r| > \sqrt{D_r/T_{\text{obs}}}. \tag{30}$$

This effectively sets a lower limit on the sensitivity of the system to drift.

7. A simple example

As a simple example, consider an anisotropic, axisymmetric diffusive medium as shown in figure 4. Within the plane, the diffusion rate is $D_\parallel$, and perpendicular to the plane, the diffusion rate is $D_\perp$. While the orientation of the plane is shown perpendicular to the vertical (z) axis in the laboratory frame, in practice, one would not generally know the orientation of the principal axes of the diffusion tensor. The diffusion tensor in this example is:

$$\bar{\bar{\mathbf{D}}} = \begin{bmatrix} D_\parallel & 0 & 0 \\ 0 & D_\parallel & 0 \\ 0 & 0 & D_\perp \end{bmatrix}. \tag{31}$$

Consider probing the sample with beams at angles θ_i with respect to the vertical axis and a wave vector of length k_0. The wave vector $\mathbf{k}_i = k_0\,(\hat{\mathbf{z}}\cos\theta_i + \hat{\mathbf{x}}\sin\theta_i)$ (because of axial symmetry). Then β_i may be calculated as:

$$\begin{aligned} \beta_i &= -4\mathbf{k}_i^T \bar{\bar{\mathbf{D}}} \mathbf{k}_i \\ &= -4k_0^2\,(\hat{\mathbf{z}}\cos\theta_i + \hat{\mathbf{x}}\sin\theta_i)^T \left(D_\parallel \hat{\mathbf{x}}\hat{\mathbf{x}}^T + D_\perp \hat{\mathbf{z}}\hat{\mathbf{z}}^T\right)(\hat{\mathbf{z}}\cos\theta_i + \hat{\mathbf{x}}\sin\theta_i) \\ &= -4k_0^2\,(\hat{\mathbf{z}}\cos\theta_i + \hat{\mathbf{x}}\sin\theta_i)^T \left(D_\parallel \sin\theta_i \hat{\mathbf{x}} + D_\perp \cos\theta_i \hat{\mathbf{z}}\right) \\ &= -4k_0^2\left(D_\parallel \sin^2\theta_i + D_\perp \cos^2\theta_i\right). \end{aligned} \tag{32}$$

For example, if the sample is probed at two angles θ_1 and θ_2, the solution is found by solving the following linear system:

$$\begin{bmatrix} \beta_1 \\ \beta_2 \end{bmatrix} = -4k_0^2 \begin{bmatrix} \cos^2\theta_1 & \sin^2\theta_1 \\ \cos^2\theta_2 & \sin^2\theta_2 \end{bmatrix} \begin{bmatrix} D_\perp \\ D_\parallel \end{bmatrix}. \tag{33}$$

8. DT-OCT simulations of an anisotropic collagen matrix

Here we employed Monte Carlo simulations of anisotropic diffusion to explore the sensitivity of the proposed DT-OCT method for quantifying pore anisotropy in ECM. To provide relevant context for the simulation, we employed input parameters consistent with our previous study of fibroblast-mediated remodeling of artificial ECM (collagen:Matrigel) using DLS-OCT with gold nanorod probes (Blackmon *et al* 2016). In that study we showed a proportionality between the apparent ECM pore size by SEM and the nanorod diffusion rate by DLS-OCT when averaged over the culture. Yet, evidence of increasing heterogeneity in both SEM and DLS-OCT, and evidence of patchy ECM fiber alignment in SEM (as in figure 1), suggested that the lack of ability to resolve

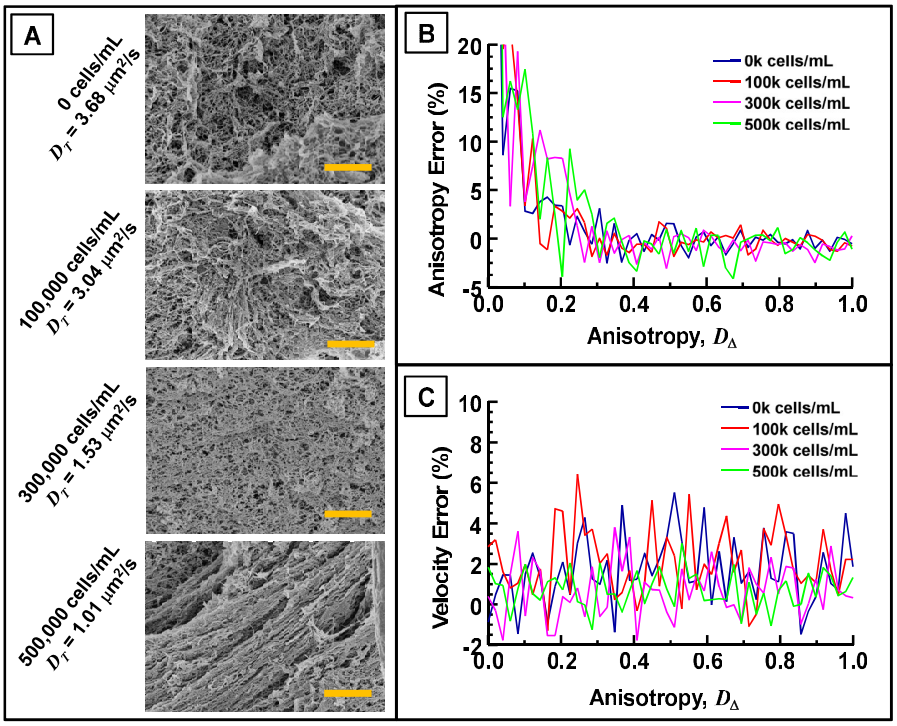

Figure 5. (A): SEM images of artificial ECM 48 h after seeding with RMF cells of varying densities, with average translational diffusion rates (D_T) of nanorods in each culture from Blackmon *et al* (2016). (B) and (C): error in diffusion tensor anisotropy (D_Δ) and drift velocity magnitude, respectively, of simulated measurements using D_{ISO} equal to D_T from each of the culture conditions. (Scalebar = 3 μm).

$D_{\|}$ and $D_{\perp}$ prevented accurate interpretation of the ECM remodeling. As such, DT-OCT may be useful for understanding this model system.

To simulate the data collection we matched the image acquisition parameters of our existing DLS-OCT system (Blackmon *et al* 2016), including an illumination wavelength of 800 nm, a sample refractive index of 1.34 (as of water), a sampling rate (A-line rate) of 25 kHz, 4000 samples per M-scan, 12 particles per coherence volume, and 3 M-scans per illumination direction (analogous to our previous method of averaging the autocorrelations of 3 adjacent rows of a single M-scan). Since we are not concerned with the rotational motion of the nanorods that were employed previously, here we treat spherical diffusive probes with translational diffusion rates set to equal those of the nanorods (i.e. of identical hydrodynamic diameter). Unlike the simple example above, we wanted to simulate an unknown tilt angle of the sample; the tilt angle (i.e. the tilt of the principle z axis of the sample's diffusion tensor) was set to 25° from the laboratory z' axis. The NA was set to 0.8, and measurements were simulated using 6 incident optical beams at angles given by the optimal solution presented in section 5. The diffusion tensor and velocity vector were extracted by fitting the simulated OCT measurements according to equation (23). To fit the logarithmic derivative β_i, the following sum was calculated with $\Delta\tau$ being the separation between samples of the autocorrelation, N_A being the number of samples, and log is the complex logarithm taken over the principal branch between $-i\pi$ to $i\pi$:

$$\beta_i = \frac{\sum_{n=0}^{N_A-2} |\Gamma_i(\mathbf{k}_i,(n+1)\Delta\tau)\Gamma_i(\mathbf{k}_i,n\Delta\tau)| \log\left[\frac{\Gamma_i(\mathbf{k}_i,(n+1)\Delta\tau)}{\Gamma_i(\mathbf{k}_i,n\Delta\tau)}\right]}{\Delta\tau \sum_{n=0}^{N_A-2} |\Gamma_i(\mathbf{k}_i,(n+1)\Delta\tau)\Gamma_i(\mathbf{k}_i,n\Delta\tau)|}. \tag{34}$$

A weighting is applied so that values of the autocorrelation for which there is little signal available, namely toward larger τ, contribute less to the estimate of the complex decay constant. Each experimental condition was simulated 50 times to estimate the mean and standard deviation of the simulated measurement.

To simulate nanoparticle diffusion, particles were uniformly randomly seeded within a 3D cube of one wavelength and displaced in time with a Gaussian random step size given by their diffusion rate along each of the 3 principle axes of the diffusion tensor. While this simulation is of nanoparticles, DT-OCT does not require a contrast agent and can be used with endogenous light scatterers as well. To simulate ECM anisotropy, we assumed a uniaxial diffusion tensor $D_x = D_y = D_{\perp}$ and $D_z = D_{\|}$ and defined the diffusion tensor anisotropy D_Δ and an effective isotropic diffusion rate D_{ISO} using the conventions previously developed in NMR (Eriksson *et al* 2015):

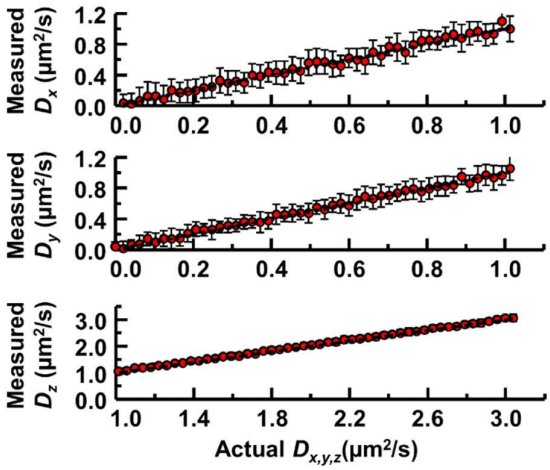

Figure 6. Simulated measured diffusion rates by DT-OCT versus the underlying actual diffusion rate used in the simulation along the principle axes *x*, *y*, and *z*. Anisotropy was swept from 0 to 1 for a fixed average diffusion rate D_{ISO} matched to that from nanorods diffusing in artificial ECM seeded with reduction mammoplasty fibroblasts. The dotted line indicates measured = actual.

$$D_{\Delta} = \frac{D_z - (D_x + D_y)/2}{D_{\mathrm{ISO}}}$$
$$D_{\mathrm{ISO}} = (D_x + D_y + D_z)/3. \tag{35}$$

D_{ISO} was chosen to match that of nanorods obtained by our previous DLS-OCT study from artificial ECM cultures seeded with increasing numbers of fibroblasts (Blackmon *et al* 2016). Specifically, D_{ISO} was set to the spatially-averaged nanorod diffusion rate in 1:1 collagen:Matrigel cultures measured at 48 hours after being seeded with 0, 100 000, 300 000, and 500 000 fibroblasts cm^{-3}, which were 3.68 $\mu\mathrm{m}^2\mathrm{s}^{-1}$, 3.04 $\mu\mathrm{m}^2\ \mathrm{s}^{-1}$, 1.53 $\mu\mathrm{m}^2\mathrm{s}^{-1}$, and 1.01 $\mu\mathrm{m}^2\mathrm{s}^{-1}$, respectively. Subsequently, $D_{\parallel}$ and $D_{\perp}$ were computed for varying anisotropies D_{Δ} swept from 0 (isotropic) to 1 (fully anisotropic). While we do not anticipate significant particle flow in this model system, to demonstrate the robustness of the measurements in the presence of drift, we also simulated a background flow field of $v_x = 15\ \mu\mathrm{m\ s}^{-1}$, $v_y = -7.5\ \mu\mathrm{m\ s}^{-1}$, $v_z = 11.25\ \mu\mathrm{m\ s}^{-1}$.

It is important to note that the range of diffusion and velocity values explored in the simulations meet the four criteria described in section 6. While we did not explicitly model the finite nature of the coherence volume, according to equation (27) the total observation time $T_{\mathrm{obs}} = 0.16$ s is shorter than the shortest particle transit time of 0.35 s given a coherence length of 6 μm. Second, the sampling rate of 25 kHz is faster than the maximum speckle decorrelation rate of 5.1 kHz calculated using equation (28). Third, according to equation (29), at the lowest isotropic diffusion rate (1.01 $\mu\mathrm{m}^2\mathrm{s}^{-1}$) simulated, the observation time should be $\gg$0.0085 s, which is satisfied. However, the simulation does scan over values of D_x and D_y that approach zero, where the impact on the measurement accuracy is discussed below. Fourth, the minimum measurable drift velocity is 0.14 $\mu\mathrm{m\ s}^{-1}$ according to equation (30), which is well below the simulated flow field components.

We note that in a practical scenario, the M-mode image acquisition time (comprised of 4000 A-lines) would be approximately 0.2 s, including the recording time (0.16 s) and time to move the scanning beam and begin another image (0.04 s). This corresponds to a total DT-OCT measurement time (six M-mode images) of 1.2 s, while noting that parallel OCT (Barrick *et al* 2016) might be beneficial to parallelize DT-OCT acquisition over multiple volumes.

Figure 5 presents the error in simulated measurements of diffusion tensor anisotropy and the magnitude of the drift velocity for each experimental condition. For anisotropy $D_{\Delta} > 0.3$, the measured D_{Δ} is within 5% error. For $D_{\Delta} < 0.3$, the difference between actual versus measured D_{Δ} exceeds 10%, which is expected as $D_{\parallel}$ and $D_{\perp}$ approach the same value (become degenerate), and the error in $D_{\parallel}$ begins to more significantly influence the calculated anisotropy. This behavior is predicted from eigenvalue perturbation theory, as even a small perturbation in the diffusion tensor due to measurement error tends to repel nearly degenerate eigenvalues, known as the avoided crossing effect (Griffiths 1995, Anderson 2001). In contrast, the drift velocity errors are generally below 6% and independent of D_{Δ}. Interestingly, drift velocity measurements are on average more accurate when D_{T} is lower (i.e. for the more highly concentrated cell cultures). This effect is attributed to the fact that drift will comprise a greater proportion of particle transport relative to diffusion when D_{T} is lower, thus lowering the drift velocity sensitivity according to equation (30).

The simulated measurements of diffusion rates in each of the *x*, *y*, and *z* directions (in the sample frame) for the 500 000 fibroblasts/cm^3 culture are presented in figure 6. This demonstrates that DT-OCT is capable of

resolving the individual diffusion tensor eigenvalues across a range of anisotropies when the sample is arbitrarily tilted relative to the measurement beam (noting that the fitting code was blind to the tilt angle). However, it is interesting to note that the standard deviation of D_x measurements was significantly larger than that of D_y or D_z (0.14 $\mu m^2 s^{-1}$ versus 0.11 $\mu m^2 s^{-1}$ and 0.10 $\mu m^2 s^{-1}$, respectively). Additional simulations were performed to determine that this effect arises from the larger angle between the x axis and the optic axis (90°), in comparison to that for the y and z axes (65° and 25°, respectively). Importantly, the size scale of these standard deviations suggest an overall diffusion rate sensitivity on the order of 0.1 $\mu m^2\ s^{-1}$, which corresponds to a speckle decorrelation time of 0.03 s. This is at the threshold of violating the criterion of equation (29) where the T_{obs} used of 0.16 s is not sufficiently long to provide averaging over many decorrelation events.

These results using realistic laboratory acquisition parameters demonstrate that DT-OCT is viable for spatially-resolved measurements that would be necessary to fully understand tissue properties. Specifically, we show how DT-OCT could measure accurate diffusion tensor components and anisotropy over ranges of diffusion rates obtained for nanoparticles diffusing in artificial ECM in previous experiments, with a simulated measurement time of 1.2 s and spatial resolution of 6 μm. These simulation results demonstrate DT-OCT as a promising tool for measuring the directions and rates of diffusion and velocity of particles throughout ECM.

9. Conclusion

This manuscript lays the framework for DT-OCT, which is presented as a minimally invasive method of measuring the diffusion tensor and velocity vector of particles. Here, we have demonstrated its potential for measuring ECM pore anisotropy via Monte Carlo simulations. The ability to non-invasively quantify the pore anisotropy offers several applications for biomedicine. One is the potential to non-invasively measure the porous nanostructure of mammary ECM as relevant to tumor growth. Another is to monitor directional-dependent motility of intracellular scatterers, which is a predictor of cell migration and is influenced by forces on the cell, chemotaxis, and durotaxis (Zhong *et al* 2014). Additionally, DT-OCT could aid in tissue engineering to monitor both microvascular networks and ECM restructuring simultaneously (Piterina *et al* 2009). DT-OCT may also aid in assessing delivery of nanocarrier-based drugs (Ferruz and De Fabritiis 2016).

DT-OCT also offers the ability to study biopolymeric liquids. For example, our laboratory has previously investigated the porosity of mucus as it relates to pulmonary diseases (Chhetri *et al* 2014, Blackmon *et al* 2017). DT-OCT offers a new ability to quantity anisotropy of biopolymers under stress, which in the case of mucus, affects its performance as a lubricant and barrier (Lai *et al* 2009).

Here, we treated GNRs as nanospheres since we were only concerned with translational diffusion. In the future, this DT-OCT model will be extended to diffusion of anisotropic particles, including rotational and translational motions. Anisotropic particles are advantageous for studying tissue properties, since many have shape-dependent optical properties that can be used to tune probes for tissue contrasting and with other OCT methods, including spectroscopic and photothermal OCT (Oldenburg *et al* 2016). Additionally, the information obtained from knowing both translational and rotational particle motion has potential for elucidating particle transport within more highly confined structures, as opposed to the weakly-constrained regime discussed here. These nano-rheological measurements are complementary to larger-scale micro-rheological measurements that measure bulk tissue properties, and coupled with directional motion information could elucidate the dynamics of collagen cross-linking, and its role in tissue stiffness and porosity.

In summary, DT-OCT is a novel approach to measuring diffusion tensors and velocity vectors of nanoparticles, with the potential for impacts in several areas of biomedicine.

Acknowledgments

We acknowledge Victoria Madden in the Microscopy Services Laboratory at UNC for her assistance in acquiring and interpreting the SEM images reported in this manuscript. This work has been supported by funds from the National Institutes of Health via R21HL111968, R21CA179204, and R21HL130901 (Oldenburg) and the National Science Foundation via the NSF Career Award CBET 1351474 (Oldenburg).

ORCID iDs

Amy L Oldenburg https://orcid.org/0000-0002-2642-8350

References

Ajeti V, Nadiarnykh O, Ponik S M, Keely P J, Eliceiri K W and Campagnola P J 2011 Structural changes in mixed col i/col v collagen gels probed by shg microscopy: implications for probing stromal alterations in human breast cancer *Biomed. Opt. Express* **2** 2307–16

Akhtar R, Schwarzer N, Sherratt M, Watson R, Graham H, Trafford A, Mummery P and Derby B 2009 Nanoindentation of histological specimens: mapping the elastic properties of soft tissues *J. Mater. Res.* **24** 638–46
Anderson A W 2001 Theoretical analysis of the effects of noise on diffusion tensor imaging *Magn. Reson. Med.* **46** 1174–88
Assoian R K and Klein E A 2008 Growth control by intracellular tension and extracellular stiffness *Trends Cell Biol.* **18** 347–52
Barcus C E, Keely P J, Eliceiri K W and Schuler L A 2013 Stiff Collagen Matrices Increase Tumorigenic Prolactin Signaling in Breast Cancer Cells *J. Biol. Chem.* **288** 1272
Barrick J, Doblas A, Gardner M R, Sears P R, Ostrowski L E and Oldenburg A L 2016 High-speed and high-sensitivity parallel spectraldomain optical coherence tomography using a supercontinuum light source *Opt. Lett.* **41** 5620–3
Basser P J, Mattiello J and LeBihan D 1994 Mr diffusion tensor spectroscopy and imaging *Biophys. J.* **66** 259–67
Blackmon R, Kreda S, Sears P, Chapman B, Hill D, Tracy J, Ostrowski L and Oldenburg A 2017 Direct monitoring of pulmonary disease treatment biomarkers using plasmonic gold nanorods with diffusion-sensitive OCT *Nanoscale* **9** 4907–17
Blackmon R L, Sandhu R, Chapman B S, Casbas-Hernandez P, Tracy J B, Troester M A and Oldenburg A L 2016 Imaging extracellular matrix remodeling *in vitro* by diffusion-sensitive optical coherence tomography *Biophys. J.* **110** 1858–68
Boas D, Bizheva K and Siegel A 1998 Using dynamic low-coherence interferometry to image brownian motion within highly scattering media *Opt. Lett.* **23** 319–21
Camp J T, Elloumi F, Roman-Perez E, Rein J, Stewart D A, Harrell J C, Perou C M and Troester M A 2011 Interactions with fibroblasts are distinct in basal-like and luminal breast cancers *Mol. Cancer Res.* **9** 3–13
Chhetri R K, Blackmon R L, Wu W-C, Hill D B, Button B, Casbas-Hernandez P, Troester M A, Tracy J B and Oldenburg A L 2014 Probing biological nanotopology via diffusion of weakly constrained plasmonic nanorods with optical coherence tomography *Proc. Natl Acad. Sci.* **111** E4289–97
Chhetri R K, Kozek K A, Johnston-Peck A C, Tracy J B and Oldenburg A L 2011 Imaging three-dimensional rotational diffusion of plasmon resonant gold nanorods using polarization-sensitive optical coherence tomography *Phys. Rev.* E **83** 040903
Cox T R and Erler J T 2011 Remodeling and homeostasis of the extracellular matrix: implications for fibrotic diseases and cancer *Dis. Models Mech.* **4** 165–78
Eriksson S, Lasič S, Nilsson M, Westin C-F and Topgaard D 2015 NMR diffusion-encoding with axial symmetry and variable anisotropy: distinguishing between prolate and oblate microscopic diffusion tensors with unknown orientation distribution *J. Chem. Phys.* **142** 104201
Falzon G, Pearson S and Murison R 2008 Analysis of collagen fibre shape changes in breast cancer *Phys. Med. Biol.* **53** 6641
Fercher A F, Drexler W, Hitzenberger C K and Lasser T 2003 Optical coherence tomography—principles and applications *Rep. Prog. Phys.* **66** 239
Ferruz N and De Fabritiis G 2016 Binding kinetics in drug discovery *Mol. Inf.* **35** 216–26
Gentle J E 2007 *Matrix Algebra—Theory, Computations, and Applications in Statistics* (New York: Springer)
Goodman J W 1996 *Introduction to Fourier Optics* (New York: McGraw-Hill)
Griffiths D J 1995 *Introduction to Quantum Mechanics* (Upper Saddle River, NJ: Prentice Hall)
Hasan K M, Parker D L and Alexander A L 2001 Comparison of gradient encoding schemes for diffusion-tensor MRI *J. Magn. Reson. Imaging* **13** 769–80
Hidalgo-Tobon S 2010 Theory of gradient coil design methods for magnetic resonance imaging *Concepts Magn. Reson.* A **36A** 223–42
Jones D P, Hanna W, El-Hamidi H and Celli J P 2014 Longitudinal measurement of extracellular matrix rigidity in 3d tumor models using particle-tracking microrheology *J. Vis. Exp.* **88** 51302
Lai S K, Wang Y-Y, Wirtz D and Hanes J 2009 Micro-and macrorheology of mucus *Adv. Drug Deliv. Rev.* **61** 86–100
Le Bihan D, Mangin J-F, Poupon C, Clark C A, Pappata S, Molko N and Chabriat H 2001 Diffusion tensor imaging: concepts and applications *J. Magn. Reson. Imaging* **13** 534–46
Lee J, Wu W, Jiang J Y, Zhu B and Boas D A 2012 Dynamic light scattering optical coherence tomography *Opt. Express* **20** 22262–77
Leitgeb R, Hitzenberger C K and Fercher A F 2003 Performance of fourier domain versus time domain optical coherence tomography *Opt. Express* **11** 889–94
Levental K R *et al* 2009 Matrix crosslinking forces tumor progression by enhancing integrin signaling *Cell* **139** 891–906
Mattiello J, Basser P and Lebihan D 1994 Analytical expressions for the b matrix in {NMR} diffusion imaging and spectroscopy *J. Magn. Reson.* A **108** 131–41
Melhem E R, Mori S, Mukundan G, Kraut M A, Pomper M G and van Zijl P C M 2002 Diffusion tensor MR imaging of the brain and white matter tractography *Am. J. Roentgenol.* **178** 3–16
Mori S and Tournier J-D 2014 *Introduction to Diffusion Tensor Imaging and Higher Order Models* (Oxford: Academic)
Mori S and Zhang J 2006 Principles of diffusion tensor imaging and its applications to basic neuroscience research *Neuron* **51** 527–39
Mukherjee P, Berman J, Chung S, Hess C and Henry R 2008 Diffusion tensor mr imaging and fiber tractography: theoretic underpinnings *Am. J. Neuroradiol.* **29** 632–41
Oldenburg A L, Blackmon R L and Sierchio J M 2016 Magnetic and plasmonic contrast agents in optical coherence tomography *IEEE J. Sel. Top. Quantum Electron.* **22** 133–45
Paszek M J *et al* 2005 Tensional homeostasis and the malignant phenotype *Cancer Cell* **8** 241–54
Piterina A, Callanan A, Davis L, Meaney C, Walsh M and McGloughlin T 2009 Extracellular matrices as advanced scaffolds for vascular tissue engineering *Bio-Med. Mater. Eng.* **19** 333–48
Popescu G, Dogariu A and Rajagopalan R 2002 Spatially resolved microrheology using localized coherence volumes *Phys. Rev.* E **65** 041504
Popov I, Weatherbee A S and Vitkin I A 2014 Dynamic light scattering arising from flowing brownian particles: analytical model in optical coherence tomography conditions *J. Biomed. Opt.* **19** 127004
Provenzano P P, Eliceiri K W, Campbell J M, Inman D R, White J G and Keely P J 2006 Collagen reorganization at the tumor-stromal interface facilitates local invasion *BMC Med.* **4** 38
Ralston T S, Marks D L, Carney P S and Boppart S A 2006 Inverse scattering for optical coherence tomography *J. Opt. Soc. Am.* A **23** 1027–37
Wolf K, Te Lindert M, Krause M, Alexander S, Te Riet J, Willis A L, Hoffman R M, Figdor C G, Weiss S J and Friedl P 2013 Physical limits of cell migration: control by ecm space and nuclear deformation and tuning by proteolysis and traction force *J. Cell Biol.* **201** 1069–84
Zhong Y, He S, Dong C, Ji B and Hu G 2014 Cell polarization energy and its implications for cell migration *C. R. Mec.* **342** 334–46